Research Article | Vol. 33, No. 2 / 27 Jan 2025 / Optics Express 2115

Optics EXPRESS

Dual-polarization O-band silicon photonics transmitter with an integrated tunable laser, Mach-Zehnder modulators, and SOAs

JUNQIAN LIU,[1,*] AARON WISSING,[1] HECTOR ANDRADE,[1] AARON MAHARRY,[1] STEPHEN MISAK,[1] GIOVANNI GILARDI,[2] GUAN-LIN SU,[2] RANJEET KUMAR,[2] MARIO MILICEVIC,[3] LARRY A. COLDREN,[1] ADEL A. M. SALEH,[1] JAMES F. BUCKWALTER,[1] AND CLINT L. SCHOW[1]

[1]*Department of Electrical and Computer Engineering, University of California Santa Barbara, Santa Barbara, CA 93106, USA*
[2]*Integrated Photonic Solutions, Intel Corp., 2200 Mission College Blvd, Santa Clara, CA 95054, USA*
[3]*MaxLinear Incorporated, 50 Parker, Irvine, CA 92618, USA*
[*]*junqian@ucsb.edu*

Abstract: Presented is an O-band silicon photonics dual-polarization coherent/IMDD modulator integrated with semiconductor optical amplifiers and tunable laser to enhance the short-reach link budget. The laser demonstrated output power >6 dBm and a <250 kHz linewidth over a 14 nm tuning range. Modulators paired with custom 64 Gbaud QPSK drivers exhibited improved analog link sensitivity compared to similar devices without integrated gain sections. They also demonstrated 53 Gbaud dual-polarization PAM4 operation when characterized with a linear driver and MaxLinear 100G/lane DSP board. Both optical links achieved BERs at the KP4-FEC threshold and overall transmitter assembly energy consumption <6.9 pJ/bit without any thermal control when at steady room temperatures.

1. Introduction

Energy-efficient short-reach optical interconnects will be necessary to meet future data center network demands driven by the exponential growth of AI training requirements. Dual-polarization (DP) intensity-modulation direct-detection (IMDD) offers a viable and cost-effective solution to double current fiber capacity by using both polarization states for optical modulation [1,2]. Higher spectral efficiency and relatively low cost of implementation make DP-IMDD attractive for applications where high link budget is not essential, such as for typical short-reach optical links. However, the introduction of optical circuit switches (OCS) into the lower spline blocks of data center networks, motivated by the potential to achieve up to 3x improvements in system availability and model-dependent performance [3], challenges IMDD link budget requirements.

By leveraging phase and polarization of optical signals, coherent detection achieves increased data rates per wavelength while enabling higher optical link budgets to allow for lower level OCS in data center networks by mixing the modulated signal with a local oscillator (LO) laser [4,5]. The link budget is further improved for both coherent and IMDD schemes by minimizing photonic integrated circuit (PIC) coupling losses with integrated gain sections to remove the need for complex packaging of externally coupled components [6,7].

This work presents a silicon photonics transmitter (Tx) with integrated gain sections, enabling the use of heterogeneously integrated lasers and semiconductor optical amplifiers (SOA), typically unavailable on monolithic silicon PICs. The paper first outlines laser characterization followed by modulator design principles. The transmitter's standalone coherent performance was then validated by biasing it for polarization-multiplexed carrier, quadrature phase-shift keying (QPSK)

#543911 https://doi.org/10.1364/OE.543911
Journal © 2025 Received 7 Oct 2024; revised 15 Nov 2024; accepted 22 Nov 2024; published 15 Jan 2025

and connecting it to a commercial receiver (Rx). Finally, DP-PAM4 operation was demonstrated using a Thorlabs photoreceiver and commercially available MaxLinear IMDD DSP boards.

2. Transmitter component characteristics

Transmitter PICs were fabricated on Intel's silicon photonics platform which heterogeneously integrates InP active material through plasma-assisted bonding [6,8] and has been successfully proven in many previous IMDD applications for short-reach links [9,10]. The platform was used to design and fabricate a DP-coherent Tx with integrated gain sections for the laser and SOAs seen in the circuit diagram of Fig. 1 and physical assembly in Fig. 2. Monitoring photodetectors (PD) were included in the unused output of each 2x2 multimode interferometer (MMI) to simplify the procedures for biasing each arm's thermal phase shifters.

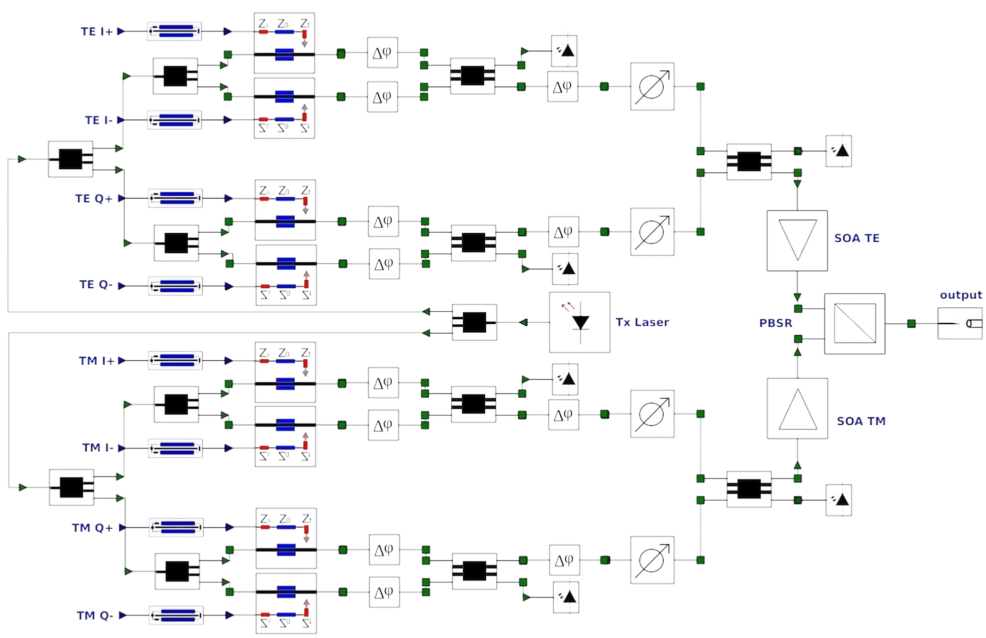

Fig. 1. Block diagram illustrating the components used in the transmitter PIC.

2.1. Integrated laser and amplifiers

The SOAs using this quantum well active material have previously been reported with a noise figure of 6 dB and gain of 15 dB [10]. The laser in this demonstration was designed with a Sagnac loop as the front reflector and 1x3 multimode interference (MMI) structures as back reflectors [11,12]. Light-current (LI) sweeps determined a laser threshold current of approximately 8 mA when at steady room temperatures of ~ 20°C. Measurements obtained from an optical spectrum analyzer (OSA), shown in Fig. 3(a), indicate a sidemode suppression ratio (SMSR) greater than 40 dB and a tuning range of 14 nm with 2 nm channel spacing.

The laser was biased at 70 mA to provide 5 mW of optical input power per polarization arm while the MZM was biased for maximum transmission in all arms. The Tx output power was measured at the edge facet using a 9/125 single-mode fiber tapered as an AR coated lens with a 2 μm spot size and 10 μm working distance. During the polarization power sweeps shown in Fig. 3(b), the SOA bias current for each measured polarization channel was swept while the other SOA was reverse biased to absorb optical power, allowing independent measurement of

Optics EXPRESS

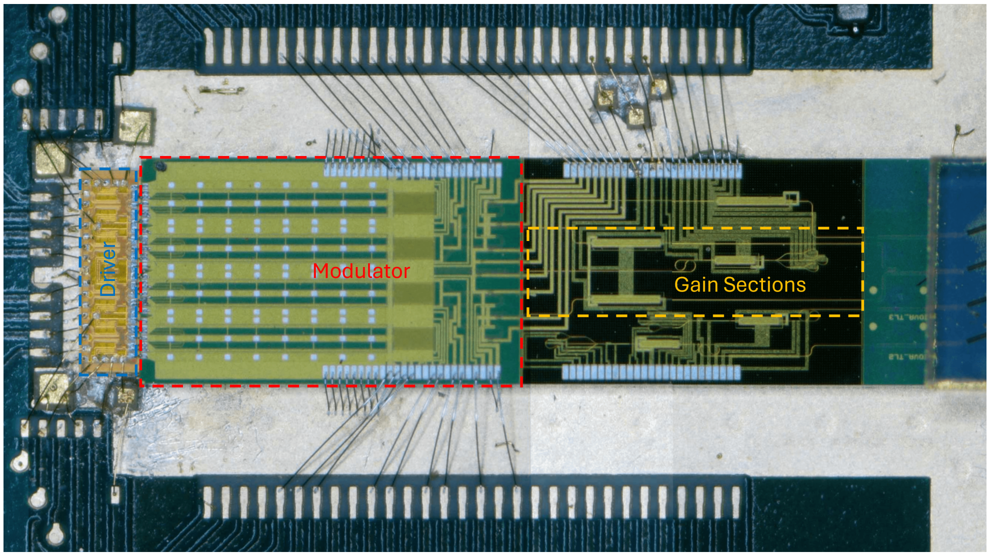

Fig. 2. Micrograph of the full transmitter assembly consisting of the 1.5 mm long driver wire bonded to the 12.5 mm long PIC on a single PCB. Both chips are 3.3 mm wide and had several DC traces bonded to small decoupling capacitors.

fiber-coupled power from both polarization channels. Minor asymmetries between channels were likely caused by fabrication tolerances and SOA spacing differences relative to the laser, which introduce different levels of thermal crosstalk. The maximum fiber coupled output power achieved was 2.5 mW for each polarization channel, with negligible polarization-dependent loss (PDL). Note that physically the actual on-chip polarization is TE only until one IQ branch is rotated and combined by the polarization beam combiner (PBC) following the output SOAs.

Linewidth was characterized by connecting the Tx output to a 2 km delayed self-heterodyne setup consisting of a 200 MHz Brimrose AOM (AMF-200-1310-2FP-SM) and Finisar photodetector (XPDV2320R). As shown in Fig. 4(a), the resulting line shape had an apparent 500 kHz full width at half maximum (FWHM) or a 250 kHz FWHM when accounting for self-beating.

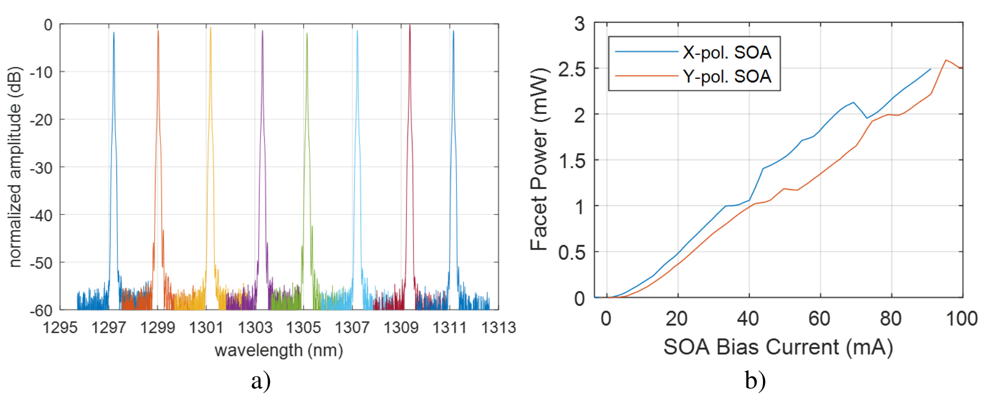

Fig. 3. a) Normalized laser frequency spectrum on the OSA showing a wavelength tuning range of 1297-1311 nm. b) SOA injection current for each individual polarization channel measured against Tx facet output power, coupled through lensed fiber with the integrated laser turned on.

Additionally, an OEWaves 4000 noise analyzer measured a -153 dBc/Hz relative intensity noise (RIN) floor and 3 kHz^2/Hz white frequency noise floor shown in Fig. 4(b). This spectrum was also confirmed with a frequency noise discriminator measurement previously used to characterize ultra low-noise lasers [13]. The white noise floor was much lower than the self-heterodyne linewidth because of the analyzer's shorter integration times and lack of mechanical noise introduced by the fiber spool delay line. Spurious spikes in the noise spectrum are likely caused by technical noise, such as the fiber coupler's mechanical stage, rather than being intrinsic to the laser. All measurements were performed without active temperature control, relying solely on passive cooling provided by an aluminum stage and thermal paste on the PCB backside.

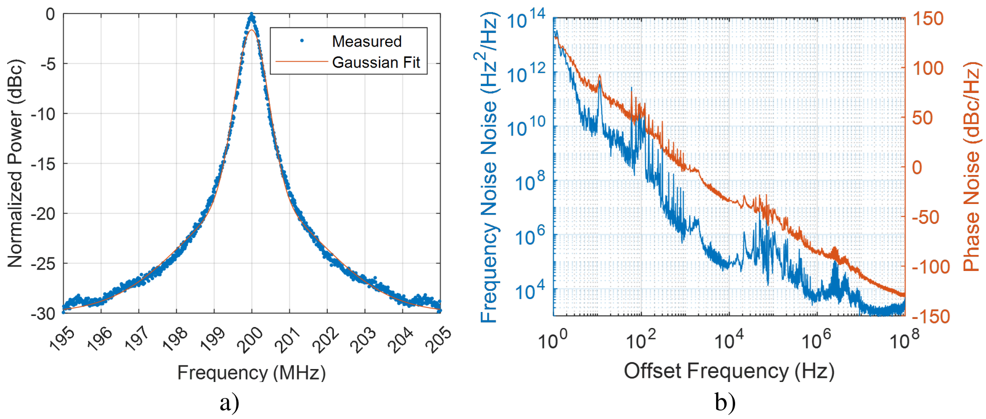

Fig. 4. a) Self-heterodyne linewidth measurement with an apparent FWHM of 200 kHz. b) Frequency and phase noise power spectral density plots measured with an OE4000.

2.2. Modulator

The modulator design consists of four differential pairs of traveling-wave Mach-Zehnder modulators (TW-MZM) that rely on silicon PN junction phase shifters operating in depletion mode and implemented in silicon-on-insulator (SOI) rib waveguide structures. Initially, various dopant implant layers were modeled using Sentaurus Process simulations, which were calibrated against measured secondary ion mass spectroscopy (SIMS) profiles. Subsequently, transfer length method (TLM) structures were measured to extract the sheet resistance values for various doping conditions. This data was then used to calibrate the relationship between carrier mobility and doping concentration, taking into account potential fabrication and material defects. Although detailed calibration methods for these initial steps are beyond the scope of this paper, they have been thoroughly covered in previous studies [14–17].

After these calibrations, the PN junction profiles were exported to Lumerical CHARGE to obtain diode junction impedance per unit length, denoted Y_{PN}. This voltage-dependent equivalent circuit was modeled as a varactor [18], which includes several key components: PN contact resistance R_{PN}, slab base capacitance C_{slab}, rib top resistance R_{rib} and capacitance C_{rib}.

To accurately determine these circuit elements, AC frequency sweeps were performed at fixed bias levels. These were used to identify depletion width pinch-off voltages, which must be avoided to ensure proper modulation of the PN junction. An example of a pinch-off condition is illustrated in Fig. 5 where the upper part of the waveguide exhibits high resistance, leading to reduced efficiency in high-speed modulation. This effect can be modeled as the circuit drawn in Fig. 6. With the assumption that the $s^2 R_{rib} C_{slab} C_{rib}$ term is negligible over the MZM's operating

Optics EXPRESS

frequencies, the impedance can be approximated as

$$\begin{aligned} Z_{PN} &= R_{PN} + \frac{1}{sC_{slab}} \parallel (R_{rib} + \frac{1}{sC_{rib}}) \\ &\simeq R_{PN} + \frac{1 + sR_{rib}C_{rib}}{s(C_{slab} + C_{rib})} \end{aligned} \tag{1}$$

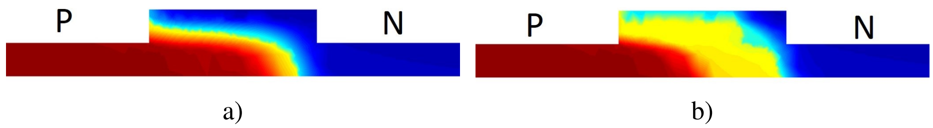

Fig. 5. PN junction net charge profiles exemplifying pinch-off conditions, which were avoided in the final design. They are displayed as signed logarithmic scale, with red regions indicating more holes and blue regions as more electrons. The depletion region, colored yellow, shows (a) no pinch-off and (b) pinch-off occurring at the N-contact.

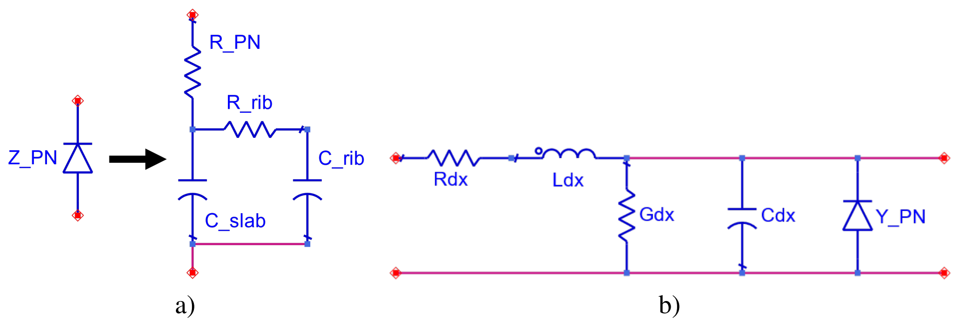

Fig. 6. a) PN junction equivalent circuit model used to match voltage and frequency simulations from Lumerical CHARGE. b) Travelling wave electrode model using frequency dependent RLGC parameters loaded by PN junction varactor admittance.

Note that when pinch-off does not occur, the resistance R_{rib} approaches zero, simplifying the expression to a common RC series model which was the case for the actual junction designs simulated and fabricated in the following sections. Figure 7 shows real and imaginary errors of the circuit model when fitted to the AC impedance of the example PN junction. The errors increase from less than 1% to 15% at higher frequencies due to substrate parasitics. However, such effects were already accurately captured by electrode RLGC extraction and should be disregarded in the junction impedance model, as including them would overestimate RF losses.

The differential traveling-wave electrodes were calibrated by measuring S-parameters on PN-loaded and unloaded cutback structures and compared to their corresponding Ansys HFSS simulations. Simulations of frequency-dependent RLGC parameters for these short segments were combined with voltage-dependent PN junction conductance and cascaded in PathWave ADS using appropriate line terminations to determine electrode S_{21} and microwave index. Optical characteristics were obtained by exporting the net charge density mesh for each bias condition to Lumerical MODE, which enabled the calculation of effective index and optical loss [19]. These parameters were then combined with the microwave index to determine the velocity mismatch penalty on the electro-optic S_{21} [20,21]. Finally, bias-dependent electro-optic responses were integrated with custom driver circuit simulations to perform transient optical modulation amplitude (OMA) and bit error ratio (BER) simulations at 56 Gb/s NRZ. These simulations served as the primary figure-of-merit (FOM) for optimizing the performance of all the devices. The simulated QPSK limiting driver in this case was a custom differential design fabricated in GlobalFoundries 9HP 90 nm SiGe BiCMOS process [22–24].

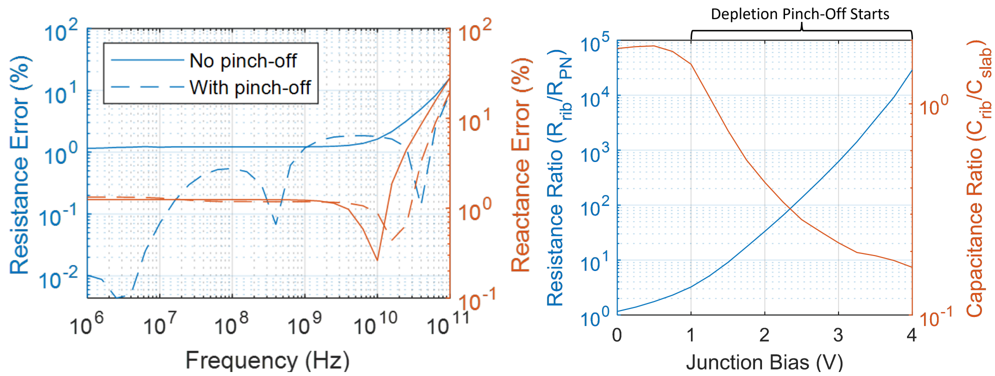

a) b)

Fig. 7. Impedance simulation results of the example junction profiles fitted to the proposed circuit model. a) Percentage errors of real and imaginary components between the circuit model and simulated impedance during frequency sweeps. b) RC ratios between the slab and rib regions are displayed as a function of the applied voltage.

Finalized simulations are presented in Fig. 8. The EO response was peaked to improve high frequency performance by optimizing the driver's built-in equalization and setting the termination resistance to be slightly lower than the transmission line impedance [13,25,26]. Additionally, AC-coupling capacitors were integrated between the resistor and ground lines to allow larger junction reverse biases without dissipating DC power through the terminations. The junction profiles were also designed to prevent pinch-off across the entire bias range, as such conditions introduce additional nonlinearities. Only bondwire inductance and bondpad capacitance were included so spurious oscillations caused by the IC's post-layout parasitics were not captured by the simulation. Other factors independent of the driver and MZM co-design, such as optical noise, fabrication tolerances, and receiver performance were found to have a relatively minor impact on the overall optimal design parameters.

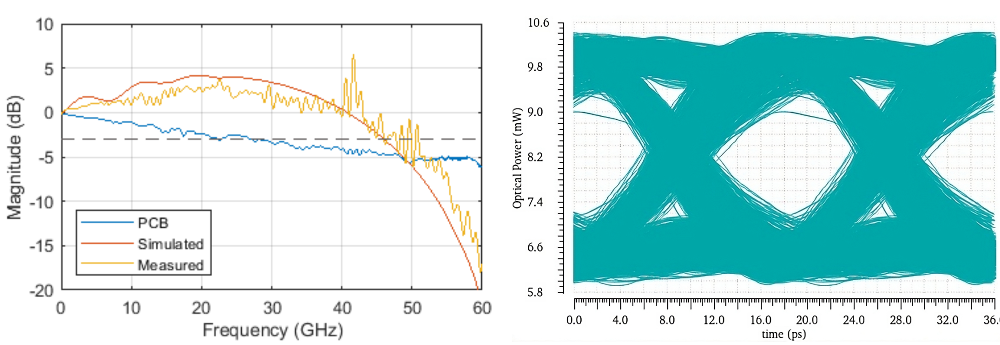

a) b)

Fig. 8. a) Tx EO bandwidth simulation versus de-embedded S_{21} measurement with extra oscillations due to driver layout parasitics. b) Transient EO eye diagram simulation for optimized Tx design at 56 Gb/s NRZ with a 10 mW optical input.

One fabricated TW-MZM PIC was wire bonded to the QPSK driver on a custom Tachyon 100G PCB as a complete transmitter assembly shown in Fig. 2. The N4373C lightwave component

Optics EXPRESS

analyzer measured an overall 3 dB EO bandwidth of ~ 45 GHz when PCB packaging parasitics were de-embedded from S-parameters in Fig. 8(a). The small-signal performance remained consistent with no noticeable differences between devices with and without integrated gain sections. It was also found that this single-ended S_{21} had negligible differences from differential ones due to differential crosstalk being isolated by thick ground traces.

3. Data transmission measurements

The Tx was initially validated by QPSK polarization-multiplexed carrier measurements. In this setup, the unmodulated arm was rotated to TM polarization by the integrated PBC before the fiber coupler. It served as the forwarded carrier for the local oscillator (LO) port, maintaining a constant power of 310 μW per PD [27]. The Tx output was fiber coupled to a commercial polarization splitter rotator equipped with linear polarizers before being fed into the reference 90° hybrid (Kylia COH28X-FCAPC-1300nm) outputting to a pair of balanced photodetectors (Finisar BPDV3320R). The praseodymium-doped fiber amplifier (PDFA) compensated for the absence of a dedicated LO and transimpedance amplifier (TIA) in the Rx test setup as depicted in Fig. 9. Note that full dual-polarization results are presented in another experiment outside the scope of this work as accurately de-embedding the Tx characteristics from the optical Rx and coherent DSP was not possible [28].

Path length differences between the receiver LO and signal input ports were minimized to enhance IQ phase stability. Repeating pseudo-random binary sequence (PRBS) 15 words were generated using a bit pattern generator (BPG-SHF 12105A) and transmitted to the Tx PCB through 4-inch SMP cables. On the Rx side, a 256 GSa/s real-time oscilloscope (RTO-UXR0702A) was configured for 1 μs acquisition windows to collect bits. Notably, Tx temperature control, digital signal processing (DSP) equalization, and carrier recovery were not required in any of the subsequent coherent experiments. The ambient room temperature was a steady ~ 20°C, while the Tx PCB settled at a maximum of 29°C after 25 min for a lasing wavelength of 1305.1 nm. Significant improvements in coupling and thermal stability could be made by packaging devices in standardized form-factor pluggables, but the required resources were unavailable for this demonstration.

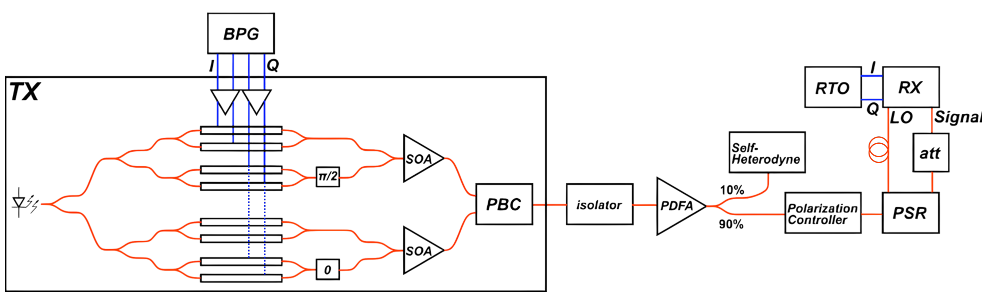

Fig. 9. Block diagram of the transmitter with on-chip laser and self-homodyne test setup. Polarization carrier multiplexing biases the LO branch to the peak and QPSK signal to null output power, while dual polarization IMDD maximized power in the outer differential arms connected to the BPG and minimized power in the unused inner arms. (i.e. BPG Q is channel switched to the dashed lines.)

The QPSK drivers received a differential input swing of 1.6 V_{ppd} for a 2 V_{ppd} output while reverse biasing the junctions to 3.5 V. Resulting constellations in Fig. 10 were generally consistent with previous single-polarization transmission demonstrations using external optical sources, however a faulty differential channel in the BPG caused IQ swings to be imbalanced [22–24]. The observed BER improvements in Fig. 11 were primarily due to reduced fiber path length

Optics EXPRESS

mismatch between the LO and signal paths, along with the use of a lower-noise laser source, despite a 3 dB reduction in power to the Rx LO port and BPG swing penalty. The driver and Tx PIC consumed 3.7 pJ/bit and 2.9 pJ/bit, respectively, resulting in an overall assembly power efficiency of 6.6 pJ/bit per channel at 64 Gbaud, excluding the external PDFA. BERs below the KP4-FEC threshold were achieved across all specified data rates at maximum signal power.

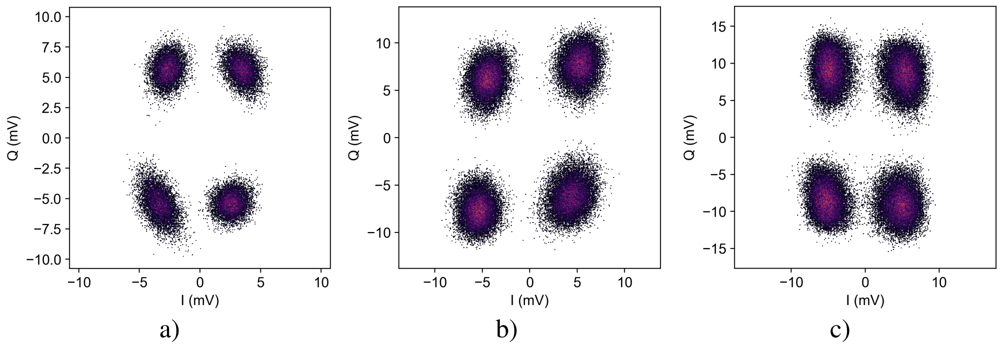

Fig. 10. QPSK constellations at a) 28, b) 56, and c) 64 Gbaud with the lowest BER in the sensitivity curves. IQ swing imbalance resulted from a faulty BPG channel.

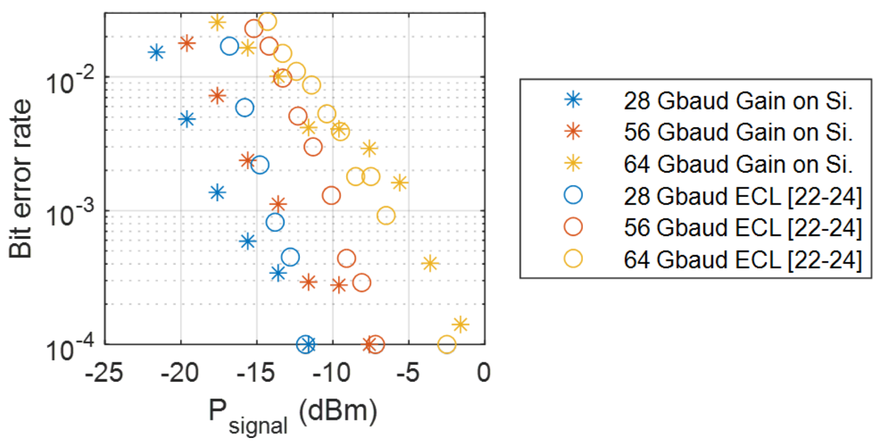

Fig. 11. Sensitivity curves with (*) and without (o) integrated gain sections on silicon measured at 64, 56, and 28 Gbaud against total received signal power at the Rx hybrid.

For PAM4 measurements, the PIC was bonded to a Marvell IN6426DZ linear driver. The BPG and RTO were replaced with a MaxLinear Keystone 800G DSP evaluation kit, operating at 53.125 Gbaud for single and dual-polarization modes. The Thorlabs RXM40AF optical receiver was configured with a differential gain of 1.6 V/mW and bandwidth of 27 GHz thus removing the need for an external PDFA. BERs were calculated by the DSP board in a 5-second capture window. For accurate clock recovery and signal integrity, the it could only capture samples within the open portion of the eye diagram, where decision levels are clearly distinguishable. Fig. 12 plots the eye diagrams recovered from both TE and TM channels under best case conditions while Fig. 13(a) combines 10^5 samples from each condition into condensed histograms.

The BER corresponding to each eye diagram, along with the ratio level mismatch (RLM) of the histograms [29], is summarized in Table 1. In single-polarization operation, a slight mismatch in linearity is observed between the channels since the RLM was optimized for

Optics EXPRESS

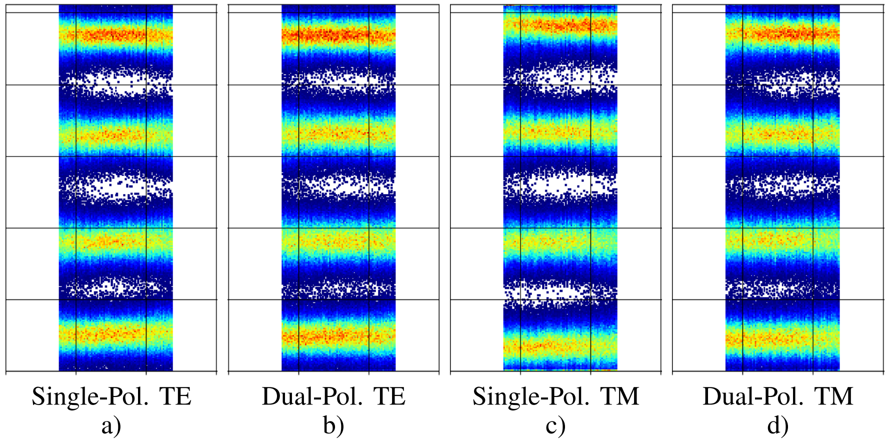

Fig. 12. Normalized PAM4 eye diagrams retrieved from the Keystone DSP measuring both data channels under single and dual polarization conditions. Note that a) and c) have less noisy eye openings than b) and d) due to the lack of polarization crosstalk.

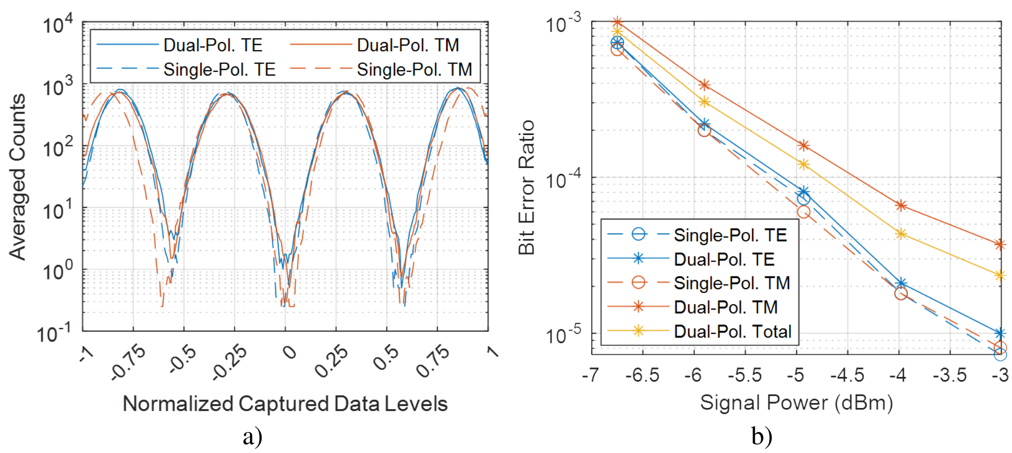

Fig. 13. PAM4 histograms used to estimate the RLM of each polarization channel under dual and single polarization conditions with maximum signal power.

dual-polarization operation. This was likely due to a minor polarization crosstalk imbalance caused by polarization-dependent loss (PDL) in the components and test equipment. However, it results in only a minor BER power penalty of less than 1.5 dB between the TE and TM channels, as illustrated by the BER curve in Fig. 13(b). The penalty did not significantly degrade the BER for either channel, as the highest recorded BER was $5.0 \cdot 10^{-5}$ for the TM channel during dual-polarization operation.

The overall energy efficiency of 6.9 pJ/bit per channel for this Tx assembly variant included the extra optical power directed into unused quadrature arms when biased for dual-polarization IMDD and excludes power consumption of the Thorlabs Rx. Future improvements could be made by integrating 2x2 optical switches at the IQ splitter, either to reduce the power consumed by the laser or to increase the net link budget. Furthermore, BER performance could be further improved by employing a receiver with an integrated polarization control loop, which would dynamically minimize polarization crosstalk [30]. Future studies should explore packaging these

Optics EXPRESS

assemblies into a pluggable form factor that improves fiber coupling stability and ensures reliable performance under realistic thermal conditions in data centers [31].

Table 1. IMDD PAM4 Summarized Results

Modulation format	Dual-Pol. TE	Dual-Pol. TM	Single-Pol. TE	Single-Pol. TM
RLM [29]	0.9905	0.9528	0.8483	0.9646
Norm. Min. Level Separation	0.3365	0.3396	0.3175	0.3363
Norm. Max. Level Separation	0.3365	0.3491	0.3839	0.3451
Min. BER	1.2e-5	5.0e-5	1.1e-5	1.0e-5

4. Conclusion

We have reported a silicon photonics coherent transmitter operating at O-band with integrated gain sections enabling an on-chip hybrid laser and optical amplifiers. 128 Gb/s (64 Gbaud) QPSK transmission was demonstrated with a polarization-multiplexed carrier scheme, which results in a Tx assembly energy efficiency of ~ 6.6 pJ/bit per channel while maintaining better link budgets than devices without integrated gain. Dual-polarization PAM4 using commercially available DSP also achieved a total data rate of 212 Gb/s (53 Gbaud) with ~ 6.9 pJ/bit per channel energy efficiency. All experiments achieved BERs below KP4-FEC thresholds without active thermal control at steady ambient room temperature, thus demonstrating the potential for integrated gain material on silicon photonics to meet the increasingly demanding link budgets of short-reach optical interconnects. However, lifetime reliability studies of these assemblies in standardized pluggable packages should be done to confirm commercial viability in more realistic environments with larger temperature variations.

Funding. Advanced Research Projects Agency - Energy (9458057).

Acknowledgments. Views and opinions of authors expressed herein do not necessarily state or reflect those of the United States Government or any agency thereof. The authors would like to thank: Intel Silicon Photonics and Intel Labs for assistance with design; Intel F11X for fabrication; V. V. Kumar and C. Kretzschmar at GlobalFoundries for support with IC fabrication; Alethea Butler-Nalin for wire bonding; Joel Guo from Bower's lab for the OEwaves measurements; and Kaikai Liu from Blumenthal's lab for the frequency noise discriminator confirmation.

Disclosures. The authors declare no conflicts of interest.

Data availability. Data underlying the results presented in this paper are not publicly available at this time, but may be obtained from the authors upon reasonable request.

References

1. M. Morsy-Osman, M. Chagnon, M. Poulin, *et al.*, "224Gb/s 10km transmission of PDM PAM4 at 1.3m using a single intensity-modulated laser and direct-det. MIMO DSP receiver," J. Lightwave Technol. **33**(7), 1417–1424 (2015).
2. C. R. Doerr, "Dual-polarization direct-detection for data-center optical communications," *Next-Generation Optical Communication: Components, Sub-Systems, and Systems XII*, vol. 12429 (SPIE, 2023), pp. 222–225.
3. H. Liu, R. Urata, K. Yasumura, *et al.*, "Lightwave fabrics: at-scale optical circuit switching for datacenter and machine learning systems," in *SIGCOMM*, (Assoc. for Comp. Machinery, New York, NY, USA, 2023), pp. 499–515.
4. T. Hirokawa, S. Pinna, N. Hosseinzadeh, *et al.*, "Analog coherent detection for energy efficient intra-data center links at 200 Gbps per wavelength," J. Lightwave Technol. **39**(2), 520–531 (2021).
5. J. Cheng, C. Xie, Y. Chen, *et al.*, "Comparison of coherent and IMDD Transceivers for Intra Datacenter Optical Interconnects," in *Opt. Fiber Comms. Conf.*, (Optica Publishing Group, 2019), p. W1F.2.
6. R. Jones, P. Doussiere, J. B. Driscoll, *et al.*, "Heterogeneously Integrated InP\/silicon photonics: fabricating fully functional transceivers," IEEE Nanotechnology Mag. **13**(2), 17–26 (2019).
7. A. Maharry, H. Andrade, S. Misak, *et al.*, "Integrated SOAs enable energy-efficient intra-data center coherent links," Opt. Express **31**(11), 17480–17493 (2023).
8. D. Pasquariello and K. Hjort, "Plasma-assisted InP-to-Si low temperature wafer bonding," IEEE J. Sel. Top. Quantum Electron. **8**(1), 118–131 (2002).
9. H. Yu, D. Patel, W. Liu, *et al.*, "800 Gbps fully integrated silicon photonics transmitter for data center applications," in *Opt. Fiber Comms. Conf.*, (2022), pp. 1–3.

Optics EXPRESS

10. S. Fathololoumi, C. Malouin, D. Hui, *et al.*, "Highly integrated 4 Tbps silicon photonic IC for compute fabric connectivity," in *IEEE Symposium on High-Performance Interconnects*, (2022), pp. 1–4. ISSN: 2332–5569.
11. G.-L. Su and M. C. Wu, "Widely tunable semiconductor lasers with three interferometric arms," Opt. Express **25**(18), 21400–21409 (2017).
12. G.-L. Su, M. N. Sakib, J. Heck, *et al.*, "A heterogeneously-integrated III-V/silicon interferometric widely tunable laser," in *Advanced Photonics Congress*, (Optica, 2019), p. IW3A.1.
13. K. Liu and D. J. Blumenthal, "Integrated Brillouin laser in 4-meter-coil resonator realizing 40 mW output power and 31 mHz fundamental linewidth," in *CLEO 2024*, (2024), p. STh4O.4.
14. G. Queirolo, E. Servida, L. Baldi, *et al.*, "Dopant activation, carrier mobility, and TEM studies in polycrystalline silicon films," J. Electrochem. Soc. **137**(3), 967–971 (1990).
15. G. Masetti, M. Severi, and S. Solmi, "Modeling of carrier mobility against carrier concentration in arsenic-, phosphorus-, and boron-doped silicon," IEEE Trans. Electron Devices **30**(7), 764–769 (1983).
16. M. Finetti, R. Galloni, and A. M. Mazzone, "Influence of impurities and crystalline defects on electron mobility in heavily doped silicon," J. Appl. Phys. **50**(3), 1381–1385 (1979).
17. K. H. Nicholas, "Implantation damage in silicon devices," J. Phys. D: Appl. Phys. **10**(4), 393–407 (1977).
18. Analog Modeling, in *The Designer's Guide to Verilog-AMS*, K. S. Kundert and O. Zinke, eds. (Springer US, Boston, MA, 2004), The Designer's Guide Book Series, pp. 35–98, 1st ed.
19. M. Nedeljkovic, R. Soref, and G. Z. Mashanovich, "Free-carrier electrorefraction and electroabsorption modulation predictions for silicon over the 1–14um infrared wavelength range," IEEE Photonics J. **3**(6), 1171–1180 (2011).
20. M. Nazarathy, D. W. Dolfi, and R. L. Jungerman, "Velocity-mismatch compensation in traveling-wave modulators using pseudorandom switched-electrode patterns," J. Opt. Soc. Am. A **4**(6), 1071–1079 (1987).
21. Modulators, in *Semiconductor Devices for High-Speed Optoelectronics*, G. Ghione, ed. (Cambridge University Press, Cambridge, 2009), pp. 356–439.
22. A. Maharry, J. Liu, S. Misak, *et al.*, "First demonstration of an O-Band coherent link for intra-data center applications," in *European Conference on Optical Communication (ECOC)*, (2022), pp. 1–4.
23. A. Maharry, S. Misak, H. Andrade, *et al.*, "A 224 Gbps/? O-Band coherent link for intra-data center applications," in *Opt. Fiber Comms. Conf.*, (Optica Publishing Group, 2023), p. M1E.5.
24. A. Maharry, J. Liu, S. Misak, *et al.*, "First demonstration of an O-Band coherent link for intra-data center applications," J. Lightwave Technol. **41**(21), 6643–6650 (2023).
25. H. Andrade, J. Liu, T. Hirokawa, *et al.*, "Optical transmitter equalization with tunable mismatched terminations in a silicon modulator," IEEE Photonics Technol. Lett. **34**(15), 775–778 (2022).
26. A. Mohammadi, S. Levasseur, and W. Shi, "Impedance peaking in silicon traveling wave Mach-Zehnder modulators," in *CLEO*, (Optica Publishing Group, 2023), p. JW2A.130.
27. J. Liu, A. Maharry, A. Wissing, *et al.*, "First O-band silicon coherent transmitter with integrated hybrid tunable laser and SOAs," in *Silicon Photonics XVIII*, vol. 12426 (SPIE, 2023), pp. 66–70.
28. S. Misak, A. Wissing, J. Zhang, *et al.*, "400 Gbps/?DP-16QAM O-band link with SiP TX and RX PICs using only heterogeneously integrated lasers and SOAs for optical gain," in *Opt. Fiber Comms. Conf.*, (2024), p. Th4C.5.
29. *IEEE Standards for Ethernet* (IEEE Standards Association, 2022).
30. X. Wu, D. Huang, T. Kim, *et al.*, "Integrated dual-polarization silicon photonic transceiver with automated polarization control," in *Opt. Fiber Comms. Conf.*, (2023), pp. 1–3.
31. P. Notaro, Q. Yu, S. Haeri, *et al.*, "An optical transceiver reliability study based on SFP monitoring and OS-level metric data," in *International Symposium on Cluster, Cloud and Internet Computing*, (IEEE/ACM, 2023), pp. 1–12.